

Open Research Online

The Open University's repository of research publications and other research outputs

Retention of inherited Ar by alkali feldspar xenocrysts in a magma: Kinetic constraints from Ba zoning profiles

Journal Item

How to cite:

Renne, Paul R.; Mulcahy, Sean R.; Cassata, William S.; Morgan, Leah E.; Kelley, Simon P.; Hlusko, Leslea and Njau, Jackson (2012). Retention of inherited Ar by alkali feldspar xenocrysts in a magma: Kinetic constraints from Ba zoning profiles. *Geochimica et Cosmochimica Acta*, 93 pp. 129–142.

For guidance on citations see [FAQs](#).

© 2012 Elsevier Ltd.

Version: Accepted Manuscript

Link(s) to article on publisher's website:

<http://dx.doi.org/doi:10.1016/j.gca.2012.06.029>

Copyright and Moral Rights for the articles on this site are retained by the individual authors and/or other copyright owners. For more information on Open Research Online's data [policy](#) on reuse of materials please consult the policies page.

oro.open.ac.uk

Accepted Manuscript

Retention of inherited Ar by alkali feldspar xenocrysts in a magma: Kinetic constraints from Ba zoning profiles

Paul R. Renne, Sean R. Mulcahy, William S. Cassata, Leah E. Morgan, Simon P. Kelley, Leslea Hlusko, Jackson Njau

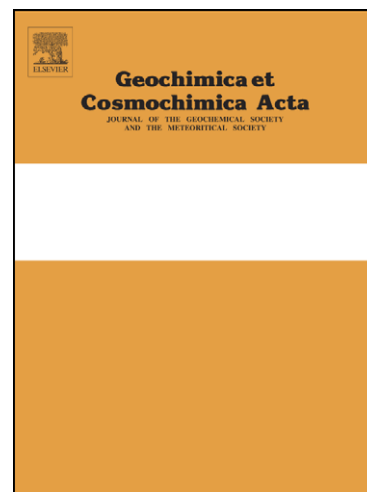
PII: S0016-7037(12)00391-2
DOI: <http://dx.doi.org/10.1016/j.gca.2012.06.029>
Reference: GCA 7813

To appear in: *Geochimica et Cosmochimica Acta*

Received Date: 10 April 2012
Accepted Date: 28 June 2012

Please cite this article as: Renne, P.R., Mulcahy, S.R., Cassata, W.S., Morgan, L.E., Kelley, S.P., Hlusko, L., Njau, J., Retention of inherited Ar by alkali feldspar xenocrysts in a magma: Kinetic constraints from Ba zoning profiles, *Geochimica et Cosmochimica Acta* (2012), doi: <http://dx.doi.org/10.1016/j.gca.2012.06.029>

This is a PDF file of an unedited manuscript that has been accepted for publication. As a service to our customers we are providing this early version of the manuscript. The manuscript will undergo copyediting, typesetting, and review of the resulting proof before it is published in its final form. Please note that during the production process errors may be discovered which could affect the content, and all legal disclaimers that apply to the journal pertain.



1 **Retention of inherited Ar by alkali feldspar xenocrysts in a magma: Kinetic**
2 **constraints from Ba zoning profiles**

3

4 **Paul R. Renne^{1,2}, Sean R. Mulcahy², William S. Cassata^{1,2}, Leah E. Morgan², Simon P.**
5 **Kelley³, Leslea Hlusko⁴, and Jackson Njau⁴**

6 ¹Berkeley Geochronology Center, 2455 Ridge Road, Berkeley, California 94709, USA

7 ²Department of Earth and Planetary Science, University of California, Berkeley, California
8 94720, USA

9 ³Department of Earth Sciences, The Open University, Walton Hall, Milton Keynes MK7 6AA,
10 UK

11 ⁴Human Evolution Research Center, University of California, Berkeley, California 94720, USA

12

13 **Abstract**

14 ⁴⁰Ar/³⁹Ar dating of volcanic alkali feldspars provides critical age constraints on many
15 geological phenomena. A key assumption is that alkali feldspar phenocrysts in magmas
16 contain no initial radiogenic ⁴⁰Ar (⁴⁰Ar*), and begin to accumulate ⁴⁰Ar* only after
17 eruption. This assumption is shown to fail dramatically in the case of a phonolitic lava
18 from southern Tanzania that contains partially resorbed xenocrystic cores which host
19 inherited ⁴⁰Ar manifest in ⁴⁰Ar/³⁹Ar age spectra. Magmatic overgrowths on the
20 xenocrysts display variable oscillatory zoning with episodic pulses of Ba enrichment and
21 intervals of resorption. Ba concentration profiles across contrasting compositional zones
22 are interpreted as diffusion couples. Inferred temperature time histories recorded by
23 these profiles reveal significant variations between phenocrysts. Combined with Ar
24 diffusion kinetics for alkali feldspars and magma temperature inferred from two feldspar
25 thermometry, the results indicate that >1% inherited ⁴⁰Ar can be retained in such
26 xenocrysts despite immersion in magma at ~900°C for tens to >100 years. In cases where
27 the age contrast between inherited and magmatic feldspars is less pronounced, the age
28 biasing effect of incompletely degassed xenocrysts may easily go undetected.

29

30

1. INTRODUCTION

31

32 Alkali feldspars are prized for dating volcanic extrusions by the K-Ar and $^{40}\text{Ar}/^{39}\text{Ar}$
33 techniques because their high K concentrations generate measurable radiogenic ^{40}Ar ($^{40}\text{Ar}^*$)
34 accumulations even on the ka timescale (Quidelleur et al., 2001; Renne et al., 1997). It is
35 generally understood that cognate feldspars, once saturated, do not accumulate $^{40}\text{Ar}^*$ while
36 immersed in magma due to the high diffusivity of Ar in feldspars at typical magmatic
37 temperatures (i.e., $>700\text{ }^\circ\text{C}$). Whether or not xenocrystic feldspars may retain $^{40}\text{Ar}^*$ through
38 magmatic processes is not well known because magma residence times are typically poorly
39 constrained. Examples are known wherein this is inferred to be the case for plagioclase due to
40 the brevity of xenocryst entrainment, magma residence and eruption processes (Layer and
41 Gardner, 2001; Singer et al., 1998), but we are unaware of documented cases involving alkali
42 feldspars whose magmatic residence time and temperatures are known.

43 In a pioneering study, Gillespie et al. (1983, 1984) showed that alkali feldspars in granitic
44 xenoliths entrained in a basalt flow were incompletely degassed, but that some domains were
45 completely degassed and/or purged of inherited $^{40}\text{Ar}^*$ during recrystallization, enabling the age
46 of their entrainment- hence by implication the extrusion age of the lava flow- to be determined.
47 Although the plausibility of partial inherited $^{40}\text{Ar}^*$ retention in such circumstances was
48 established by Gillespie et al. (1982) based on argon diffusion parameters available at the time
49 and reasonable assumptions about the entrainment process, they did not have independent
50 constraints on the time/temperature history of the xenoliths during entrainment.

51 Rare examples of excess ^{40}Ar hosted in melt inclusions (Esser et al., 1997) and in
52 unidentified sites (Renne et al., 1997) in alkali feldspars are known. Alkali feldspar xenocrysts
53 in tuffs commonly retain inherited $^{40}\text{Ar}^*$ (Renne et al., 1999), but these are generally believed
54 to have been incorporated in late stages of eruption and/or deposition processes, hence to have
55 experienced magmatic temperatures briefly if at all.

56 This paper presents an example wherein significant amounts of inherited $^{40}\text{Ar}^*$ in alkali
57 feldspar xenocrysts were retained after entrainment in a magma. We investigate whether this is
58 consistent with independent constraints on the thermal history of the xenocrysts in the magma.
59 The sample studied is a porphyritic phonolitic lava that crops out in the Ilongo area near
60 Mbeya in southwestern Tanzania, in the general vicinity of the late Neogene Rungwe volcanics

61 (Ebinger et al., 1989). Basement rocks are not well exposed in the immediate area, but
62 presumably belong to the Ubendian shear belt, which formed episodically between 2100 and
63 1725 Ma, and was locally reactivated by Pan-African tectonism at ca. 750 Ma (Lenoir et al.,
64 1994).

65

66 **2. SAMPLE CONTEXT, PETROGRAPHY AND GEOCHEMISTRY**

67

68 The lava flow sample upon which this study is based was collected in the course of an
69 inventory of potential paleontologic resources by the Tanzanian International
70 Paleoanthropological Research Project (TIPRP) (Njau and Hlusko, 2010). The lava was
71 sampled at Lat. S 8° 47' 41.2", Long. E 33° 46' 10.6", at 1218 m elevation. The flow is poorly
72 exposed and surficially weathered, and its thickness is estimated at 3 m.

73

74 The lava is highly porphyritic, with alkali feldspar phenocrysts up to 1 cm (~15%) and smaller
75 phenocrysts of aegirine-augite (~5%), ferro-pargasite amphibole (~1%), plagioclase (<1%) and
76 euhedral titanite (<1%) set in a bluish-gray (where fresh) groundmass. The amphibole
77 phenocrysts uniformly show opacitic oxidation-resorption rims. The felty groundmass
78 comprises alkali feldspar, aegirine-augite, oxides, apatite and devitrified glass.

79

80 Many of the alkali feldspar phenocrysts contain irregularly shaped cores of another alkali
81 feldspar or plagioclase. These cores are generally visible in crossed polars through abrupt
82 discontinuities in extinction angles, but are most clearly revealed in backscattered electron
83 images (see below) because the alkali feldspar overgrowths contain distinctly higher Ba than
84 the cores.

85

86 X-ray fluorescence data obtained from the Washington State University GeoAnalytical
87 Laboratory are shown in Table 1. Chemical classification of this lava is complicated by the
88 obvious assimilation of xenocrystic feldspars and uncertain extent of major element
89 contamination, and a relatively high potential volatile content implied by the loss on ignition
90 (LOI). In the classification of Le Bas et al. (1986) it is a tephri-phonolite, but the analysis
91 normalized to a volatile-free basis corresponds to a phonolite.

92

93

3. $^{40}\text{Ar}/^{39}\text{Ar}$ RESULTS

94

95 $^{40}\text{Ar}/^{39}\text{Ar}$ analysis used methods described in Appendix A. Incremental heating of three
96 individual alkali feldspar phenocrysts (samples 34467-01, -02, and -03) produced complex
97 apparent age spectra (Figure 1a) initially rising monotonically from ca. 10-20 Ma ages for the
98 first 20-30% of the ^{39}Ar released, then increasing erratically for the remainder of each
99 experiment. Maximum apparent ages for individual steps range from ca. 200 Ma to ca. 5900
100 Ma, and integrated ages for the three crystals are 41.2 ± 0.1^1 , 96.9 ± 0.1 , and 326.5 ± 0.5 Ma. In
101 view of petrographic observations and electron microprobe results, these age spectra are
102 straightforwardly interpreted to reflect mixing between magmatic feldspar overgrowths and
103 older, incompletely degassed xenocrystic cores. In this interpretation the age of the magmatic
104 feldspar would be approximated by the initial steps at 10-20 Ma.

105

106 Two multigrain aliquots of amphibole phenocrysts were analyzed by incremental heating. Both
107 yield apparent age plateaus (Figure 1b) over 100% of the ^{39}Ar released, with indistinguishable
108 plateau ages of 17.2 ± 0.5 Ma and 17.6 ± 0.2 Ma. An isochron fit to all the data from both
109 samples yields an age of 17.9 ± 0.3 Ma, with an atmospheric $^{40}\text{Ar}/^{36}\text{Ar}$ intercept of 281 ± 9 and
110 MSWD = 0.93.

111

112 3.1. Spatial distribution of ^{40}Ar

113

114 To test the hypothesis that Ba-poor xenocrystic cores are the source of inherited Ar manifest in
115 the phenocryst age spectra, two strategies were employed.

116

117 3.3.1. Physical separation

118

119 Several phenocrysts were crushed into small fragments and heavy Ba-rich overgrowths were
120 separated from lighter Ba-poor xenocrysts based on density. Because the Ba substitution has a
121 large effect on the density of alkali feldspars (3.26 g/cm^3 for endmember $\text{BaAl}_2\text{Si}_2\text{O}_8$ versus

¹ Uncertainties here and throughout this paper are given at one standard deviation unless otherwise stated.

122 2.56 g/cm³ for endmember KAlSi₃O₈), the overgrowth feldspar was concentrated based on the
123 density contrast. Accordingly, alkali feldspar phenocrysts were crushed and sized to a 177-250
124 micron fraction, then subjected to a heavy liquid separation using dilute Li heteropolytungstate
125 (LST). The densest fraction was analyzed by total fusion of ten individual crystal fragments.
126 Nine of these proved to be alkali feldspar based on K/Ca > 10, whereas one with K/Ca = 0.056
127 ± 0.006 appears to be plagioclase. All ten crystal fragments yielded indistinguishable model
128 ages (Figure 1c) with a weighted mean of 17.53 ± 0.08 Ma, with MSWD = 0.72. An isochron
129 fit to these data yields an age of 17.55 ± 0.13 Ma, with an atmospheric ⁴⁰Ar/³⁶Ar intercept of
130 280 ± 70 and MSWD = 0.81.

131

132 The densest feldspar phenocryst (magmatic overgrowth) fragments and the hornblende
133 phenocrysts yield indistinguishable ages that are interpreted to represent the eruption age of the
134 lava. The atmospheric trapped ⁴⁰Ar/³⁶Ar ratios of both the feldspar overgrowths and the
135 hornblende phenocrysts indicates that whatever inherited “excess” ⁴⁰Ar existed in the melt was
136 efficiently exchanged with atmosphere prior to eruption. The manifest lack of inherited ⁴⁰Ar in
137 these phases would seem to preclude inherited ⁴⁰Ar in the xenocrystic cores being derived via
138 uptake from the melt, a conclusion supported by the very low partition coefficient between
139 alkali feldspars and silicate melts (Clay et al., 2011).

140

141 3.1.2. Laser probe analyses

142

143 An excimer laser was used to produce 90 μm ablation pits in the surfaces of several feldspar
144 crystals (sample 34467) and also a traverse across the surface of one crystal (Figure 2). The
145 resulting flat bottomed pits were around 10-50 μm deep. There was little significant age
146 variation and 17 analyses produced a mean age of 17.74 ± 0.33 Ma. One crystal was
147 subsequently broken to reveal the core and two traverses analyzed using the same excimer
148 laser system. In this case two of the eight ages were significantly older, reaching 71.7 ± 1.8 Ma
149 in the core of the grain. Ages in the outer 100 μm of the core fell within errors of the surface
150 ages previously measured. Based on these limited data, the two anomalously old apparent ages
151 near the center of the core are much lower than the oldest apparent ages determined in the

152 incremental heating experiments, suggesting that the laser ablation pits averaged results over a
153 relatively large region relative to the scale of the anomaly.

154

155 **3.2. Source of excess ^{40}Ar**

156

157 The eruption age of the lava is straightforwardly deduced from the indistinguishable results of
158 (i) incremental heating of amphibole phenocrysts, and analysis of alkali feldspar overgrowths
159 by (ii) physical separation, and (iii) in situ analysis by laser microprobe. The anomalously old
160 ages derived from the large alkali feldspar phenocryst fragments are clearly associated with
161 lighter, Ba-poor xenocrystic cores that are readily identified petrographically.

162 This then raises the question of how inherited Ar could be retained rather than lost by diffusion
163 at magmatic temperatures during entrainment and magma residence of the xenocrysts.

164 Addressing this question requires consideration of the specific mode of occurrence of inherited
165 $^{40}\text{Ar}^*$ in the xenocrystic cores. If the inherited $^{40}\text{Ar}^*$ is distributed in the alkali feldspar lattice,
166 then its retention should be governed by volume diffusion kinetics and the thermal histories of
167 the xenocrysts. If however the inherited $^{40}\text{Ar}^*$ is sited in inclusions, as has been inferred in
168 some alkali feldspars (Esser et al., 1997) and plagioclases (Boven et al., 2001; Jones et al.,
169 2008), such inclusions may serve as traps that retard net loss of ^{40}Ar from the composite grains
170 and thereby enhance Ar retentivity. An analogous mechanism was proposed by Shuster et al.
171 (2006) for He in radiation-damaged zones of apatite.

172

173 At least some of the inherited $^{40}\text{Ar}^*$ in the xenocrysts is clearly parentless as indicated by a
174 presolar apparent age of 5899 ± 67 Ma for one of the incremental heating steps. This
175 observation supports some finite hosting of inherited $^{40}\text{Ar}^*$ by inclusions that could act as
176 diffusion traps. Further support for this possibility may be provided by the slightly elevated Cl
177 concentrations (i.e., $^{38}\text{Ar}_{\text{Cl}}/^{39}\text{Ar}_{\text{K}}$) from the older spots analyzed by laser microprobe, although
178 the incremental heating data show no correlation between apparent age and $^{38}\text{Ar}_{\text{Cl}}/^{39}\text{Ar}_{\text{K}}$.

179

180 In the following, we address the thermal histories of the alkali feldspar xenocrysts as an
181 independent constraint for evaluating the possibility that volume diffusion failed to
182 quantitatively degas inherited $^{40}\text{Ar}^*$.

183

184

4. FELDSPAR CHEMISTRY AND XENOCRYSTS

185

186 Electron probe microanalysis (EPMA) based on methods described in Appendix B reveals that
187 the overgrowths are generally enriched in Ba, Sr, Ca and Si relative to the cores, and show
188 oscillatory zoning. The contrast between cores and overgrowths, and oscillatory zoning in the
189 latter, are especially evident in backscattered electron (BSE) images (Figure 3) which are
190 strongly sensitive to Ba concentration. A number of reconnaissance traverses were run across
191 various zones of the alkali feldspar phenocrysts and their cores as shown in Figure 4. We use
192 the shorthand GxTy to designate traverse y in grain x. In rare cases (e.g., G13 in Figure 3) the
193 xenocrystic cores are not completely mantled by overgrowths, but are separated from the melt
194 by other phenocrysts, i.e. a clinopyroxene in the case of G13.

195

196 In terms of ternary components An-Or-Ab, alkali feldspars and plagioclase are plotted in
197 Figure 5. Plagioclase data are based on core to rim traverses for two phenocrysts, and a rim-
198 core-rim traverse for a third. Alkali feldspar data, with the celsian (Cn) $\text{BaAl}_2\text{Si}_2\text{O}_8$ component
199 included with An, show that the xenocrystic cores tend to be lower in An+Cn than the
200 overgrowths, but their compositions overlap in this space.

201

202 Alkali feldspar phenocryst cores interpreted as xenocrysts are characterized by (i) irregular
203 boundaries (resorption surfaces) and (ii) low Ba (0.01-0.03 atoms per formula unit). As shown
204 by low resolution traverses (e.g., Figure 6), most crystals show several stepwise increases in Ba
205 from core to rim typically followed by more regular decreases, producing an asymmetric
206 sawtooth pattern. Ba is generally correlated with Ca, Al and Sr, and anticorrelated with Si and
207 K. Among these elements, Ba shows the largest amplitude variations relative to measurement
208 precision, hence its variations are the best resolved and most useful for diffusion modeling.

209

210 4.1. Thermometry

211

212 Determining magmatic intensive variables for the magma is complicated by the high LOI,
213 manifest xenocryst contamination, and the absence of an appropriate phase assemblage. For

214 example, at 0.1 GPa MELTS (Ghiorso and Sack, 1995) predicts liquidus temperatures of 1131
215 °C and 945 °C for f_{O_2} values at the NNO buffer for the bulk composition (i) recalculated
216 volatile-free and (ii) assigning the LOI entirely to H₂O, respectively. For the bulk composition
217 shown in Table 1, MELTS predicts alkali feldspar of appropriate Or-Ab-An composition at
218 temperatures between 970 and 1030 °C and H₂O concentrations between 0 and 0.8 wt-% at 0.1
219 GPa and NNO. However, MELTS fails to produce an amphibole or Na-Fe³⁺-rich
220 clinopyroxene under any of these conditions and the validity of temperatures inferred from
221 phase equilibria by this approach may be questionable. Opacitic rims on the amphibole attest to
222 disequilibrium with the melt upon eruption, but the argon isotopic data betray no evidence of a
223 xenocrystic origin of this phase. The clinopyroxene shows no evidence of resorption or
224 disequilibrium, and we infer that it too is a cognate phase. We conclude that the bulk
225 composition of this lava lies outside the composition space that is well-calibrated for phase
226 equilibria, and we constrain temperatures using two-feldspar thermometry as described below.

227
228 Establishing equilibrium between any particular plagioclase composition and a corresponding
229 composition of alkali feldspar is challenging. However, a relatively narrow range of
230 temperatures between 843 and 914 °C is obtained from two-feldspar thermometry (Putirka,
231 2008) by comparing both core and rim compositions of the plagioclase with the most extreme
232 compositions of alkali feldspar overgrowths. The global regression solution of (Putirka, 2008),
233 calibrated by 42 experiments, was used. A pressure of 0.3 GPa was assumed based on a
234 geothermal gradient of 30 °C/km and a maximum of 300 °C for partial retention of ⁴⁰Ar* in the
235 xenocrysts. The thermometer is insensitive to pressure between 0 GPa (876 °C) and 1.0 GPa
236 (884 °C). Tests for equilibrium (Elkins and Grove, 1990) yielded absolute values of
237 component activity differences between the two phases of <0.45 for An, <0.03 for Ab, and
238 <0.04 for Or. We take the midpoint temperature as a reasonable approximation of the average
239 temperature for alkali feldspar growth, and the extremities of temperature estimates as a
240 conservative approximation to the uncertainty. Thus we infer that alkali feldspar growth (and
241 Ba diffusion across discrete growth zone interfaces) occurred at 879 ± 36 °C, subject to the
242 assumption that high Ba concentrations do not invalidate application of the thermometer.

243

244

5. Ba DIFFUSION MODELLING

245

246 Retention of $^{40}\text{Ar}^*$ at magmatic temperatures, in light of Ar diffusion data for alkali feldspars
247 (Foland, 1974; Lovera et al., 1997; Wartho et al., 1999; Zeitler, 1987), would seem to require
248 very brief heating of the xenocrysts by the magma prior to eruption. To evaluate the duration of
249 magmatic heating, zoning profiles of trace elements across xenocryst/phenocryst feldspar
250 contacts were analyzed and interpreted as diffusion couples. Our approach is analogous to
251 several previous studies (Coombs et al., 2000; Costa and Chakraborty, 2004; Costa et al., 2003;
252 Costa and Dungan, 2005; Morgan and Blake, 2006; Morgan et al., 2006; Morgan et al., 2004;
253 Nakamura, 1995; Singer et al., 1995; Zellmer and Clavero, 2006), which were focused on
254 kinetics of magma processes in arcs and mid-ocean ridge environments. The basis is that
255 initially sharp concentration boundaries between crystal growth zones become relaxed due to
256 diffusion across the boundary in an approach to equilibrium. The extent of relaxation is
257 governed by the time, temperature, and diffusivity of the species in the medium of interest. In
258 the present case, zoning profiles of Ba were particularly useful as Ba concentrations could be
259 measured with reasonable precision and they contrast significantly across the
260 xenocryst/overgrowth contacts; moreover Ba diffusion data are available for alkali feldspars
261 (Cherniak, 2002).

262

263 Electron microprobe traverses for major elements, Ba and Sr were conducted using methods
264 described in Appendix B. Contacts between xenocrysts and overgrowths were modeled as
265 diffusion couples wherein the composition across the contact ($x=0$) is given (Crank, 1975) by:

266

$$267 \quad C(x) = \frac{C_1 + C_2}{2} + \frac{C_1 - C_2}{2} \operatorname{erf}\left(\frac{x}{2\sqrt{Dt}}\right)$$

268

269 where C_1 and C_2 ($C_2 > C_1$) are the initial concentrations on either side of the contact, D is the
270 diffusivity and t is the time duration. For each contact, a least-squares technique was used to
271 solve for the best-fit value of the composite parameter Dt .

272

273 **5.1. Excitation volume effects**

274

275 For modeling traverse results as diffusion profiles it is important to correct for the excitation
276 volume of the electron beam, which stimulates x-ray emission over a finite region that varies
277 for each element's x-ray lines with material composition and density as well as electron beam
278 energy. The averaging effect across a compositional interface produces a spuriously smooth
279 composition gradient which, unless corrected for, produces overestimation of the extent of
280 diffusion. The effect of varying beam energy for our conditions is illustrated in Figure 7. For
281 this correction (Ganguly et al., 1988) we used a Monte Carlo estimate (Jercinovic et al., 2008)
282 for the lateral spread of electrons in the sample assuming a linear density-composition
283 relationship along the $\text{BaAl}_2\text{Si}_2\text{O}_8$ - KAlSi_3O_8 join. Using this approach, a value of $\epsilon = 0.34$
284 mm was determined for a 15 kV beam, and $\epsilon = 0.05$ mm for a 10 kV beam. We used data
285 acquired solely at 10 kV for Ba diffusion modeling.

286

287 An additional complication arises when the compositional interface is inclined with respect to
288 the electron beam, i.e. is not perpendicular to the sample surface. If not accounted for, an
289 inclined interface produces bias in the inferred location of the interface and also introduces
290 asymmetry in the shape of the concentration profile, and the magnitude of both of these effects
291 depends strongly on the size of the activation volume (Arnould and Hild, 2003), hence on
292 beam energy as discussed above. For this reason, contacts visibly non-orthogonal to the plane
293 of the thin section were eschewed. Several profiles (e.g., G11T1) yielded discernible
294 asymmetry in Ba concentration profiles suggestive of inclined contacts, and these profiles were
295 not considered for diffusion modeling. Asymmetric profiles may also arise from diffusion-
296 limited initial crystal growth (Solomatov, 1995), further underscoring the need to avoid using
297 such profiles for diffusion modeling.

298

299 **5.2 Oblique traverses**

300

301 In order to increase spatial resolution, electron probe traverses were made oblique to the traces
302 of vertical contacts and the results subsequently projected onto an orthogonal traverse. This
303 was accomplished simply by multiplying traverse distance by the cosine of the angle between
304 the traverse and the normal to the interface. Contacts were determined to be vertical within an
305 estimated 10° by noting displacement of the well-defined Becke line upon racking the focus on

306 a petrographic microscope. This approach proved highly effective in increasing spatial
307 resolution without introducing any apparent bias, as shown in Figure 8. All of the data used for
308 diffusion modeling were acquired using this technique.

309

310 **5.3. Ba Dt values**

311

312 A test for the validity of the diffusion couple model is that successive contacts between
313 overgrowth zones with sharp Ba concentration contrasts should yield increasing values for the
314 cumulative quantity Dt from rim to core provided that the crystals maintain internal thermal
315 equilibrium. Although we assume that the diffusivity is temperature dependent following an
316 Arrhenius relationship, this assumption is not required for the expectation that Dt should be
317 cumulative and thus increase inwards from rim to core. This was tested affirmatively with four
318 contacts in G15 that yielded reproducible data with statistically acceptable fits (Figure 9).
319 These data indicate an initial Dt value of $2.7 \pm 0.6 \mu^2$ at the xenocryst/overgrowth boundary,
320 dropping to $0.4 \pm 0.2 \mu^2 \sim 300 \mu$ from the xenocryst margin.

321

322 The Ba Dt values of greatest interest are those between xenocrysts and the innermost
323 overgrowth layer because these reflect the maximum cumulative duration of heating of the
324 xenocrysts. Accordingly, detailed traverses across this contact were acquired for several
325 phenocrysts. Ba profiles for three of these met our reliability criteria: (i) symmetric profiles
326 implying subvertical contacts are present; (ii) consistent and unambiguous values of C_1 and C_2
327 are evident; at least 3 values intermediate between C_1 and C_2 are present; (iii) multiple
328 traverses across the same contact yield similar results. Data from multiple traverses across each
329 contact meeting these criteria were combined for a single regression.

330

331 After correction for excitation volume effects (i.e. subtraction of $0.05 \mu^2$), grains G2, G13 and
332 G15 yielded values of $Dt = 0.2 \pm 0.1$, 1.5 ± 0.3 , and $2.6 \pm 0.6 \mu^2$, respectively. It is noteworthy
333 that the Dt values correlate with the number of distinct overgrowth bands. While three
334 phenocrysts may not be representative of the whole rock, G15 has the most overgrowth layers,
335 and G2 the least, of any observed in thin section. This relationship supports a model wherein

336 the xenocrysts were entrained into the magma episodically, consistent with the heterogeneous
337 zoning patterns discussed below.

338

339 **5.4 Crystal growth rates**

340

341 Assuming isothermal conditions and using the diffusion data of Cherniak (2002), these results
342 can be used to estimate diffusion timescales for each contact. Combining these timescales with
343 measured widths of overgrowths between the contacts allows determining average crystal
344 growth rates. At 879 °C deduced from two-feldspar thermometry, the implied growth rate of
345 the innermost 108 mm of overgrowth in crystal G15 is 3.5×10^{-12} cm/s, increasing to 6.4×10^{-11}
346 cm/s for the next 189 mm. These implied rates are consistent with magmatic sanidine growth
347 rates estimated in various studies, which range from 10^{-7} to 10^{-14} cm/s (Calzolaio et al., 2010;
348 Christensen and Depaolo, 1993; Davies et al., 1994; Long, 1978; Zellmer and Clavero, 2006).

349

350 **5.5 Heterogeneous growth histories**

351

352 The compositions of successive overgrowths vary between phenocrysts although many discrete
353 compositions are common to several. For example, Figure 5 shows that crystals G2, G14 and
354 G15 have zones with ~0.06 atoms per formula unit (APFU) Ba; crystals G3, G11 and G13
355 have zones with ~0.07 APFU Ba; crystals G2, G11, G13 and G15 have zones with ~0.09
356 APFU Ba; crystals G13, G14 and G15 have zones with ~0.11 APFU Ba; crystals G11 and G15
357 have zones with ~0.13 APFU Ba.

358

359 Similarly, some overgrowth layers are recorded only locally in a given crystal. For example,
360 Figure 5 shows that G11T1 transects a zone of ~0.07 APFU Ba, whereas G11T2 traverses a
361 contact between a zone with 0.04 APFU Ba and a more rimward one with ~0.12 APFU Ba,
362 without the 0.07 APFU zone present in G11T1. The variable distribution of compositional
363 zones within and between individual phenocrysts may be partly a function of spatially variable
364 nucleation and growth, but to some extent is clearly a preservation artifact due to
365 heterogeneous resorption between growth zones. An extreme case is shown by crystal G13 in
366 Figure 3.

367

368 **5.6 Episodic crustal assimilation**

369

370 The steplike increases in Ba concentration (Figure 3) in magmatic overgrowths outward from
371 xenocryst cores are clear evidence of discrete pulses of Ba enrichment in the magma. Many of
372 the stepwise composition boundaries between xenocrystic cores and innermost overgrowths,
373 and between successive overgrowths, are partial resorption surfaces based on their irregular
374 shapes. The slow declines in Ba concentration after each sharp increase are likely the result of
375 progressive Ba depletion in the magma owing to strong partitioning into the alkali feldspar.

376

377 Ba partitioning between alkali feldspar and melt is known to be complex, with relatively strong
378 dependence on Or content of the feldspar (Icenhower and London, 1996; Mahood and Stimac,
379 1990). Our feldspars are typically 50-60 mol-% Or, thus we expect that the partition coefficient
380 to be relatively constant and likely greater than 5 (Ginibre et al., 2004). Therefore the
381 oscillatory zoning of magmatic feldspar likely reflects magma that was episodically enriched in
382 Ba. In cases where Ba-rich zones grew on resorption surfaces, Ba influx likely accompanied
383 changes in P-T-X conditions in the magma which destabilized the substrate feldspar. We
384 speculate that a likely source of Ba (and water, tending to destabilize feldspars) would be mica-
385 rich crystalline basement rocks given the strong partitioning of Ba into micas relative to other
386 silicate phases (Philpotts and Schnetzler, 1970).

387

388 No two of the analyzed crystals show identical zoning patterns. For example, G2, G3 and G15
389 all show cores with a discrete increase from ~0.2 APFU (atoms per formula unit) Ba followed
390 by large discrete increases to ~0.062, ~0.082, and ~0.071 APFU Ba (respectively). Some
391 overgrowth layers are visibly discontinuous as seen in Figure 3.

392

393 The heterogeneous growth histories presumably reflect spatially and temporally variable Ba
394 concentration in the melt and/or local variations in alkali feldspar solubility such that some
395 layers may have been precipitated and subsequently resorbed in some crystals. Whether this
396 heterogeneity reflects disequilibrium at the scale of a thin section, or late mixing of
397 phenocrysts with disparate prior histories, is unclear.

398

399

6. RETENTION OF INHERITED ARGON

400

401 We take the value of Dt determined for Ba diffusion across the innermost xenocryst-
402 overgrowth contact in each phenocryst to represent a lower bound on the time-temperature
403 history available for $^{40}\text{Ar}^*$ to diffuse out of the xenocryst, as some $^{40}\text{Ar}^*$ presumably would
404 have been degassed by conductive heating prior to entrainment. Based on available Ba
405 diffusion data (Cherniak, 2002), Dt values can be translated into square-pulse time
406 temperature-time ($T-t$) histories as shown in Figure 10. For comparison, square-pulse
407 equivalent $T-t$ curves are shown for selected fractions of $^{40}\text{Ar}^*$ lost by diffusion from the
408 xenocrysts based on the kinetic data compiled by Lovera et al. (1997) for diffusion radii
409 comparable to the dimensions of the xenocrystic cores selected for $^{40}\text{Ar}/^{39}\text{Ar}$ analysis. The
410 dimensions of cores in the crystals analyzed by $^{40}\text{Ar}/^{39}\text{Ar}$ incremental heating (e.g., as shown in
411 Figure 1a) are not known, but cores up to 2 mm are observed and the overall dimensions of
412 phenocrysts selected for the incremental heating $^{40}\text{Ar}/^{39}\text{Ar}$ analysis were larger than average.
413 More typical are cores of 0.4 to 0.8 mm dimensions, as shown in Figure 3).

414

415 We do not know the specific activation energies (E_a) or pre-exponential factors (D_0) governing
416 Ar diffusion in the xenocrystic cores. Moreover, it is possible that these parameters, as well as
417 any diffusion domain structure initially present in these feldspars, have changed due to
418 structural transformations and/or annealing in response to heating when the xenocryst was
419 entrained by the magma. Given such uncertainty, we considered values of E_a and $\log(D_0/r_0^2)$
420 one standard deviation from the mean values (46 ± 6 kcal/mol and $5 \pm 3 \log(\text{s}^{-1})$, respectively)
421 reported by Lovera et al. (1997), which is the most comprehensive study currently available on
422 Ar diffusion in alkali feldspars and includes data from orthoclase, microcline, and perthite. Ar
423 diffusion experiments using sanidine reported by Zeitler et al. (1987) fall within the range of
424 values reported by Lovera et al. (1997). Thus the data encompass a reasonable range of
425 expected diffusion parameters, although we cannot dismiss the possibility that the feldspar
426 studied herein is more or less retentive. Lovera et al (1997) suggest a value of $r_0 = 6 \mu\text{m}$ as
427 being the most relevant diffusive lengthscale to extracting D_0 from their $\log(D_0/r_0^2)$ data. In
428 modeling diffusive loss from our alkali feldspars crystals we assume the effective diffusive

429 lengthscale (r) for calculating $\log(D_0/r^2)$ from the aforementioned D_0 value is between 250 and
430 1000 microns, consistent with observations of xenocrystic core and whole-grain dimensions.

431

432 Thus, Figures 10a-c show results corresponding to the more retentive values ($E_a = 40$ kcal/mol;
433 $\log(D_0/r_0^2 = 2 \log(\text{s}^{-1}))$), and Figures 10d-f show results for the least retentive ($E_a = 52$
434 kcal/mol; $\log(D_0/r_0^2 = 8 \log(\text{s}^{-1}))$). Plane slab diffusion geometry was assumed. For each set of
435 parameters, these results provide a maximum constraint on the fraction of $^{40}\text{Ar}^*$ lost because
436 they ignore the additional diffusion distance provided by successive overgrowths on the
437 xenocrysts. The core-overgrowth relationships (based on petrography) appear epitaxial, in
438 which coherent phase boundaries are expected. Hence the margins of the xenocryst cores are
439 not expected to serve as natural diffusion boundaries and the lengthscales of whole phenocrysts
440 are logical maximum diffusion dimensions.

441

442 It is noteworthy that the dense overgrowth fragments analyzed by $^{40}\text{Ar}/^{39}\text{Ar}$ (see section 3.3.1
443 and Figure 1(c)) yielded apparent ages with only minor skew towards older ages. The
444 xenocryst/overgrowth boundaries are expected to be coherent, requiring that inherited $^{40}\text{Ar}^*$
445 diffusing out of the xenocrystic cores must diffuse through whatever overgrowths existed
446 before exiting the phenocrysts. The lack of observed excess ^{40}Ar in the overgrowth fragments
447 analyzed supports the possibility raised by the laser probe data (see section 3.1.2) that the
448 inherited $^{40}\text{Ar}^*$ has a sharply peaked spatial distribution, with peaks in the xenocrystic cores
449 and tails of very low concentrations (into the Ba-rich overgrowths). This would be enhanced by
450 a higher diffusivity of Ar in the Ba-rich overgrowths, which is possible in view of the large
451 range in kinetic parameters observed by Lovera et al. (1997).

452

453 It is also noteworthy that all of the xenocrystic cores observed are separated from the innermost
454 overgrowth layer by a resorption surface. If significant $^{40}\text{Ar}^*$ was lost from the cores prior to
455 initial overgrowth formation, and if the kinetics of resorption were faster than those of Ar
456 diffusion, as seems likely, the Ar diffusion profiles in the cores would have truncated tails prior
457 to the initial precipitation of magmatic overgrowth feldspar. Such a scenario would produce an
458 initially sharp discontinuity in $^{40}\text{Ar}^*$ concentration across the core/overgrowth contact.

459

460 Our modeling suggests that none of the T - t histories experienced by grains G2, G13 or G15 are
461 consistent with retention of significant $^{40}\text{Ar}^*$ if the Ar diffusion parameters ($E_a = 52$ kcal/mol
462 and $\log(D_0/r_0^2) = 8$) 1σ greater than the means of the Lovera et al. (1997) distributions are
463 used, even with diffusion radii at the large end of the plausible range of grain dimensions
464 (Figures 10d-f). On the other hand, if diffusion parameters ($E_a = 40$ kcal/mol and $\log(D_0/r_0^2) =$
465 2) 1σ less than the means of the Lovera et al. (1997) distribution are used (which yield lower
466 diffusivities than higher E_a values at magmatic temperatures), a core with the T - t history of
467 grain G2 would be expected to retain as much as 70% of its $^{40}\text{Ar}^*$ for any diffusion dimension
468 >250 μm , and all three T - t histories could retain $>10\%$ of their $^{40}\text{Ar}^*$ for diffusion dimensions
469 >500 μm . The possible siting of some inherited $^{40}\text{Ar}^*$ in diffusion traps as discussed previously
470 is thus permitted but not required to explain our results. We reiterate that ascribing constant
471 diffusion parameters to the core feldspars may be an oversimplification as they may have
472 undergone structural changes upon heating in the magma.

473

474 The actual fraction of $^{40}\text{Ar}^*$ retained or lost from each xenocryst is unknown without
475 information about their original Ar retention age(s). However, reasonable values can be
476 modeled. If the original age was ~ 2 Ga (Ubendian; Lenoir et al., 1994) the youngest (41.2 Ma)
477 and oldest (327 Ma) integrated ages would correspond to 99% and 90% $^{40}\text{Ar}^*$ loss,
478 respectively, assuming instantaneous loss at 17 Ma. If the original age was 750 Ma (Pan-
479 African; Lenoir et al., 1994), these values would be 95% and 60%, respectively. Thus the
480 amount of $^{40}\text{Ar}^*$ retained by the xenocrysts is consistent with the integrated ages regardless of
481 the original ages of the xenocrysts, within the wide range of possible argon diffusion
482 parameters.

483

484

7. CONCLUSIONS

485

486 Inherited $^{40}\text{Ar}^*$ is clearly associated with xenocrystic cores within alkali feldspar phenocrysts
487 in the phonolitic lava studied here. The cores unequivocally retained inherited $^{40}\text{Ar}^*$ despite
488 immersion in magma at 879 ± 36 $^\circ\text{C}$. Alkali feldspar phenocrysts in a single thin section reveal
489 diverse histories of nucleation on xenocrysts and subsequent growth histories marked by
490 episodic Ba-enrichment in the magma and instability reflected in partial resorption events. Ba

491 diffusion profiles across xenocryst/phenocryst boundaries reveal magma residence times of the
492 xenocrysts ranging from thousands to tens of thousands of days (8-110 years). Based on these
493 constraints, retention of significant and variable fractions of inherited $^{40}\text{Ar}^*$ in the xenocrysts is
494 expected for plausible values of diffusion parameters provided that diffusion lengthscales are
495 approximated by physical phenocryst dimensions. These results accord well with the results of
496 incremental heating $^{40}\text{Ar}/^{39}\text{Ar}$ experiments on individual phenocrysts.

497

498 Without knowing the actual Ar diffusion parameters in both core and overgrowth phases, their
499 specific three dimensional geometries, and the initial $^{40}\text{Ar}^*$ concentrations of the cores, it is
500 impossible to make more quantitative statements about the expected extent of $^{40}\text{Ar}^*$ retention.
501 However, we note that techniques such as x-ray tomography (Ketcham and Carlson, 2001) can
502 quantify three dimensional interior morphologies of crystals. Ba increases x-ray absorption
503 significantly and thus the strong Ba contrasts between cores and overgrowths favors the
504 possibility of mapping core-overgrowth boundaries with this technique. Mapping cores of
505 individual crystals prior to $^{40}\text{Ar}/^{39}\text{Ar}$ analysis would permit modeling with numerical diffusion
506 codes (Huber et al., 2011) capable of operating on arbitrary geometries. Such approaches
507 would likely be fruitful in cases such as we have explored here.

508

509 Inherited $^{40}\text{Ar}^*$ in alkali feldspar xenocrysts entrained in lavas is probably not be a ubiquitous
510 phenomenon, but it is probably more common than is widely supposed. The time scale of
511 magma residence inferred for alkali feldspars in some studies (Morgan et al., 2006) is shorter
512 than determined here, thus the present case is not an extreme one. Detection of the effects
513 shown here would be more difficult if the inherited components were only slightly older than
514 the magmatic event mobilizing them, as may be exemplified in alkali feldspar megacrysts in
515 the Fish Canyon Tuff (Bachmann et al., 2007) which yielded slightly but significantly older
516 ages than phenocrysts. Selection of large phenocrysts for $^{40}\text{Ar}/^{39}\text{Ar}$ dating, commonly
517 employed to maximize measurement precision, is counterproductive in such cases because the
518 retention of inherited $^{40}\text{Ar}^*$ is enhanced by an increased diffusion lengthscales.

519

520 Finally, we stress that in cases such as this where the fraction of inherited $^{40}\text{Ar}^*$ retained is
521 likely very small, uncertainties in Ar diffusion parameters are too large to permit useful

522 constraints on the kinetics of magmatic processes. What we have shown here is that within
523 such uncertainties, and in light of independent constraints posed by Ba diffusion profiles, the
524 observed retention of detectable inherited $^{40}\text{Ar}^*$ in alkali feldspar xenocrysts is plausible under
525 some realistic circumstances.

526

527 **ACKNOWLEDGMENTS**

528

529 We dedicate this paper to the late Ian S.E. Carmichael. We thank Bill Mitchell for helpful
530 suggestions; Keith Putirka for advice on use of his feldspar thermometry program; Bill Hames,
531 Paul Layer, an anonymous reviewer and Associate Editor Peter Reiners for constructive
532 reviews of the manuscript; NSF (grants EAR-0838572 and BCS-0321893) for partial support
533 of this research; and the Tanzanian Government (Commission for Science and Technology,
534 and Department of Antiquities) for fieldwork permits.

535

536 **Appendix A. $^{40}\text{Ar}/^{39}\text{Ar}$ Methods**

537

538 Samples were prepared using standard methods and facilities described elsewhere (Renne et
539 al., 1999). Samples were irradiated in the CLICIT facility of the Oregon State University
540 TRIGA reactor in two batches. The first irradiation, for 5.0 hours and using the Fish Canyon
541 sanidine (FCs) standard (Renne et al., 2010), consisted of alkali feldspar phenocrysts 3-4 mm
542 in dimension. The second batch, irradiated for 2.0 hours and using the Alder Creek sanidine
543 (ACs) standard (Nomade et al., 2005), consisted of (i) small (177-250 μ) fragments of dense
544 alkali feldspar separated via LST, and (ii) amphibole phenocrysts.

545

546 Samples were analyzed in three distinct sets of experiments. Incremental heating and single
547 crystal fusion analyses were conducted at the Berkeley Geochronology Center (BGC), and spot
548 fusion analyses with a UV laser microprobe were conducted at the Open University (OU).
549 BGC and OU data are given in electronic annexes EA-1 and EA-2, respectively.

550

551 At BGC, irradiation batch 1 and 2 samples were analyzed with MAP 215C and MAP 215-50
552 mass spectrometers (respectively), as described previously (Renne et al., 1998). Mass
553 discrimination was monitored by online analysis of air pipettes based on a power law
554 relationship (Renne et al., 2009) which gave $D = 1.00630 \pm 0.00148$ per amu for Batch 1, and
555 $D = 1.00694 \pm 0.00127$ per amu for Batch 2, each based on 29 pipettes interspersed with the
556 unknowns. Radioactive decay of ^{37}Ar and ^{39}Ar were corrected using the decay constants of
557 (Renne and Norman, 2001) and (Stoenner et al., 1965), respectively.

558

559 At OU, several grains of one sample were analysed using a Nu Noblesse mass spectrometer
560 mated to a 193 nm eximer laser system. Mass discrimination was determined by ablation of a

561 standard glass containing modern atmospheric argon indicating a discrimination factor of
562 1.0113 per amu.

563
564 Ar isotope data, corrected for backgrounds, mass discrimination and radioactive decay are
565 given in Tables EA-1 and EA-2. Apparent ages were computed from these data corrected for
566 interfering isotopes using the production ratios given by (Renne et al., 2005) and (Renne et al.,
567 2008). Ages are based on the calibration of (Renne et al., 2010), as updated by (Renne et al.,
568 2011).

569
570 In the step-heating experiments, the significance of step ages at higher fractional degassing is
571 not obvious. A presolar age of 5899 ± 67 Ma for one step clearly indicates that some of the
572 ^{40}Ar is unsupported, i.e., it is decoupled from parent ^{40}K . We hypothesize that some of the
573 $^{40}\text{Ar}^*$ degassed from the xenocryst cores diffused into K-poor voids and/or inclusions.

574 575 **Appendix B. Electron Microprobe Analysis**

576
577 Electron probe microanalysis (EPMA) was conducted with a Cameca SX-51 instrument in the
578 Dept. of Earth and Planetary Science at the University of California, Berkeley. The sample was
579 a carbon-coated polished thin section. Data acquisition, analysis, and correction procedures
580 were conducted with the software Probe for EPMA (version 8.48).

581
582 Analyses were conducted with a beam current of 10 nA and a beam diameter of 1 micron. The
583 accelerating voltage varied for some experiments as described below. In particular, to explore
584 the effects of activation volume as discussed below, several parallel traverses were run at
585 variable accelerating voltages of 10, 15 and 20 kV. Elements were acquired using the
586 analyzing crystals LIF for Fe ka, Mn ka, PET for Ti ka, Ca ka, K ka, Ba la, and TAP for Al ka,
587 Na ka, Si ka, Mg ka, Sr la. The counting time was 30 seconds for all elements. The intensity
588 data for Na ka and K ka was corrected for Time Dependent Intensity (TDI) loss (or gain) using
589 a self calibrated correction.

590
591 At 10 kV the typical detection limits (at the 99% confidence interval) in weight percent were
592 0.042 for Si, 0.018 for Al, 0.062 for Ti, 0.349 for Fe, 0.258 for Mn, 0.028 for Mg, 0.035 for
593 Ca, 0.035 for Na, 0.036 for K, 0.178 for Ba, and 0.066 for Sr. At 15k V the typical detection
594 limits (at the 99% confidence interval) in weight percent were 0.035 for Si, 0.013 for Al, 0.027
595 for Ti, 0.069 for Fe, 0.062 for Mn, 0.016 for Mg, 0.018 for Ca, 0.027 for Na, 0.019 for K,
596 0.080 for Ba, and 0.049 for Sr. At 20 k V the typical detection limits (at the 99% confidence
597 interval) in weight percent were 0.032 for Si, 0.012 for Al, 0.018 for Ti, 0.037 for Fe, 0.034 for
598 Mn, 0.013 for Mg, 0.013 for Ca, 0.027 for Na, 0.014 for K, 0.052 for Ba, and 0.041 for Sr.

599
600 The error on formula unit concentrations was determined by propagating the analytical
601 uncertainty through calculations of structural formulae (Giaramita and Day, 1990).

602

603 **REFERENCES CITED**

- 604 Arnould, O., and Hild, F., 2003. Specific effects and deconvolution in submicrometre EPMA:
605 application to binary diffusion. *X-Ray Spectrometry* 32, 345-362.
- 606 Bachmann, O., Oberli, F., Dungan, M.A., Meier, M., Mundil, R., and Fischer, H., 2007.
607 $^{40}\text{Ar}/^{39}\text{Ar}$ and U-Pb dating of the Fish Canyon magmatic system, San Juan Volcanic field,
608 Colorado: Evidence for an extended crystallization history. *Chemical Geology* 236, 134-
609 166.
- 610 Boven, A., Pasteels, P., Kelley, S.P., Punzalan, L., Bingen, B., and Demaiffe, D., 2001.
611 $^{40}\text{Ar}/^{39}\text{Ar}$ study of plagioclases from the Rogaland anorthosite complex (SW Norway); an
612 attempt to understand argon ages in plutonic plagioclase. *Chemical Geology* 176, 105-
613 135.
- 614 Calzolaio, M., Arzilli, F., and Carroll, M.R., 2010. Growth rate of alkali feldspars in
615 decompression-induced crystallization experiments in a trachytic melt of the Phlegraean
616 Fields (Napoli, Italy). *European Journal of Mineralogy* 22, 485-493.
- 617 Cherniak, D.J., 2002. Ba diffusion in feldspar. *Geochimica et Cosmochimica Acta* 66, 1641-
618 1650.
- 619 Christensen, J.N., and Depaolo, D.J., 1993. Time scales of large volume silicic magma systems
620 - Sr isotopic systematics of phenocrysts and glass from the Bishop Tuff, Long Valley,
621 California. *Contributions to Mineralogy and Petrology* 113, 100-114.
- 622 Clay, P.L., Kelley, S.P., Sherlock, S.C., and Barry, T.L., 2011. Partitioning of excess argon
623 between alkali feldspars and glass in a young volcanic system. *Chemical Geology* 289,
624 12-30. Coombs, M.L., Eichelberger, J.C., and Rutherford, M.J., 2000. Magma storage and
625 mixing conditions for the 1953-1974 eruptions of Southwest Trident Volcano, Katmai
626 National Park, Alaska. *Contributions to Mineralogy and Petrology* 140, 99-118.
- 627 Costa, F., Chakraborty, S., and Dohmen, R., 2003. Diffusion coupling between trace and major
628 elements and a model for calculation of magma residence times using plagioclase.
629 *Geochimica et Cosmochimica Acta* 67, 2189-2200.
- 630 Costa, F., and Chakraborty, S., 2004. Decadal time gaps between mafic intrusion and silicic
631 eruption obtained from chemical zoning patterns in olivine. *Earth and Planetary Science*
632 *Letters* 227, 517-530.
- 633 Costa, F., and Dungan, M., 2005. Short time scales of magmatic assimilation from diffusion
634 modeling of multiple elements in olivine. *Geology* 33, 837-840.

- 635 Crank, J., 1975. The mathematics of diffusion, Oxford, 421 p.
- 636 Davies, G.R., Halliday, A.N., Mahood, G.A., and Hall, C.M., 1994. isotopic constraints on the
637 production-rates, crystallization histories and residence times of pre-caldera silic magmas,
638 Long Valley, California. *Earth and Planetary Science Letters* 125, p. 17-37.
- 639 Ebinger, C.J., Deino, A L., Drake, R.E., and Tesha, A.L., 1989. Chronology of volcanism and
640 rift basin propagation - Rungwe volcanic province, east-Africa. *Journal of Geophysical*
641 *Research-Solid Earth and Planets* 94, 15785-15803.
- 642 Elkins, L.T., and Grove, T.L., 1990. Ternary feldspar experiments and thermodynamic models.
643 *American Mineralogist* 75, 544-559.
- 644 Esser, R.P., McIntosh, W.C., Heizler, M.T., and Kyle, P.R., 1997. Excess argon in melt
645 inclusions in zero-age anorthoclase feldspar from Mt. Erebus, Antarctica, as revealed by
646 the $^{40}\text{Ar}/^{39}\text{Ar}$ method. *Geochimica et Cosmochimica Acta* 61, 3789-3801.
- 647 Foland, K.A., 1974. ^{40}Ar diffusion in homogeneous orthoclase and an interpretation of ar
648 diffusion in k-feldspars. *Geochimica et Cosmochimica Acta* 38, 151-166.
- 649 Ganguly, J., Bhattacharya, R.N., and Chakraborty, S., 1988. convolution effect in the
650 determination of compositional profiles and diffusion-coefficients by microprobe step
651 scans. *American Mineralogist* 73, 901-909.
- 652 Ghiorso, M.S., and Sack, R.O., 1995. Chemical mass-transfer in magmatic processes .4. A
653 revised and internally consistent thermodynamic model for the interpolation and
654 extrapolation of liquid-solid equilibria in magmatic systems at elevated-temperatures and
655 pressures. *Contributions to Mineralogy and Petrology* 119, 197-212.
- 656 Giaramita, M.J., and Day, H.W., 1990. Error propagation in calculations of structural
657 formulas. *American Mineralogist* 75, 170-182.
- 658 Gillespie, A.R., Huneke, J.C., and Wasserburg, G.J., 1982. An assessment of ^{40}Ar - ^{39}Ar dating
659 of incompletely degassed xenoliths. *Journal of Geophysical Research* 87, 9247-9257.
- 660 Gillespie, A.R., Huneke, J.C., and Wasserburg, G.J., 1983. Eruption age of a pleistocene basalt
661 from ^{40}Ar - ^{39}Ar analysis of partially degassed xenoliths. *Journal of Geophysical Research*
662 88, 4997-5008.
- 663 Gillespie, A.R., Huneke, J.C., and Wasserburg, G.J., 1984. Eruption age of a approximately
664 100,000-year-old basalt from ^{40}Ar - ^{39}Ar analysis of partially degassed xenoliths. *Journal of*
665 *Geophysical Research* 89, 1033-1048.

- 666 Ginibre, C., Worner, G., and Kronz, A., 2004. Structure and dynamics of the Laacher See
667 magma chamber (Eifel, Germany) from major and trace element zoning in sanidine: A
668 cathodoluminescence and electron microprobe study. *Journal of Petrology* 45, 2197-2223.
- 669 Huber, C., Cassata, W.S., and Renne, P.R., 2011. A lattice Boltzmann model for noble gas
670 diffusion in solids: The importance of domain shape and diffusive anisotropy and
671 implications for thermochronometry. *Geochimica et Cosmochimica Acta* 75, 2170-2186.
- 672 Icenhower, J., and London, D., 1996. Experimental partitioning of Rb, Cs, Sr, and Ba between
673 alkali feldspar and peraluminous melt. *American Mineralogist* 81, 719-734.
- 674 Jercinovic, M.J., Williams, M.L., and Lane, E.D., 2008. In-situ trace element analysis of
675 monazite and other fine-grained accessory minerals by EPMA. *Chemical Geology* 254,
676 197-215.
- 677 Jones, D.A., Layer, P.W., and Newberry, R.J., 2008. A 3100-year history of argon isotopic
678 and compositional variation at El Chichon volcano. *Journal of Volcanology and*
679 *Geothermal Research* 175, 427-443.
- 680 Ketcham, R.A., and Carlson, W.D., 2001. Acquisition, optimization and interpretation of X-ray
681 computed tomographic imagery: applications to the geosciences. *Computers &*
682 *Geosciences* 27, 381-400.
- 683 Layer, P.W., and Gardner, J.E., 2001. Excess argon in Mount St. Helens plagioclase as a
684 recorder of magmatic processes. *Geophysical Research Letters* 28, 4279-4282.
- 685 Le Bas, M.J., Lemaitre, R.W., Streckeisen, A., and Zanettin, B., 1986. A chemical
686 classification of volcanic-rocks based on the total alkali silica diagram. *Journal of*
687 *Petrology* 27, 745-750.
- 688 Lenoir, J.L., Liegeois, J.P., Theunissen, K., and Klerkx, J., 1994. The Palaeoproterozoic
689 Ubendian shear belt in Tanzania - geochronology and structure. *Journal of African Earth*
690 *Sciences* 19, 169-184.
- 691 Long, P.E., 1978. Experimental determination of partition-coefficients for Rb, Sr, And Ba
692 between alkali feldspar and silicate liquid. *Geochimica et Cosmochimica Acta* 42, 833-
693 846.
- 694 Lovera, O.M., Grove, M., Harrison, T.M., and Mahon, K.I., 1997. Systematic analysis of K-
695 feldspar $^{40}\text{Ar}/^{39}\text{Ar}$ step heating results .1. Significance of activation energy determinations.
696 *Geochimica et Cosmochimica Acta* 61, 3171-3192.

- 697 Mahood, G.A., and Stimac, J.A., 1990. Trace-element partitioning in pantellerites and
698 trachytes. *Geochimica et Cosmochimica Acta* 54, 2257-2276.
- 699 Morgan, D.J., and Blake, S., 2006. Magmatic residence times of zoned phenocrysts:
700 introduction and application of the binary element diffusion modelling (BEDM)
701 technique. *Contributions to Mineralogy and Petrology* 151, 58-70.
- 702 Morgan, D.J., Blake, S., Rogers, N.W., De Vivo, B., Rolandi, G., and Davidson, J.P., 2006.
703 Magma chamber recharge at Vesuvius in the century prior to the eruption of AD 79.
704 *Geology* 34, 845-848.
- 705 Morgan, D.J., Blake, S., Rogers, N.W., DeVivo, B., Rolandi, G., Macdonald, R., and
706 Hawkesworth, C.J., 2004. Time scales of crystal residence and magma chamber volume
707 from modelling of diffusion profiles in phenocrysts: Vesuvius 1944. *Earth and Planetary*
708 *Science Letters* 222, 933-946.
- 709 Nakamura, M., 1995. Continuous mixing of crystal mush and replenished magma in the
710 ongoing Unzen eruption. *Geology* 23, 807-810.
- 711 Njau, J.K., and Hlusko, L.J., 2010. Fine-tuning paleoanthropological reconnaissance with
712 high-resolution satellite imagery: the discovery of 28 new sites in Tanzania. *Journal*
713 *of Human Evolution* 59, 680-684.
- 714 Nomade, S., Renne, P.R., Vogel, N., Deino, A.L., Sharp, W.D., Becker, T.A., Jaouni, A.R.,
715 and Mundil, R., 2005. Alder Creek sanidine (ACs-2): A Quaternary $^{40}\text{Ar}/^{39}\text{Ar}$ dating
716 standard tied to the Cobb Mountain geomagnetic event. *Chemical Geology* 218, 315-338.
- 717 Philpotts, J.A., and Schnetzler, C.C., 1970. Phenocryst-matrix partition coefficients for K, Rb,
718 Sr and Ba, with applications to anorthosite and basalt genesis. *Geochimica et*
719 *Cosmochimica Acta* 34, 307-322.
- 720 Putirka, K.D., 2008. Thermometers and Barometers for Volcanic Systems, in: Putirka,
721 K.D.T.F.J. (Ed.), *Minerals, Inclusions and Volcanic Processes*, pp. 61-120.
- 722 Quidelleur, X., Gillot, P.Y., Soler, V., and Lefevre, J.C., 2001. K/Ar dating extended into the
723 last millennium: application to the youngest effusive episode of the Teide volcano (Spain).
724 *Geophysical Research Letters* 28, 3067-3070.
- 725 Renne, P.R., Sharp, Z.D., and Heizler, M.T., 2008. Cl-derived argon isotope production in the
726 CLICIT facility of OSTR reactor and the effects of the Cl-correction in $^{40}\text{Ar}/^{39}\text{Ar}$
727 geochronology. *Chem. Geol.* 255, 463-466.

- 728 Renne, P.R., Cassata, W.S., and Morgan, L.E., 2009. The isotopic composition of atmospheric
729 argon and $^{40}\text{Ar}/^{39}\text{Ar}$ geochronology: Time for a change? *Quaternary Geochronology* 4,
730 288-298.
- 731 Renne, P.R., Knight, K.B., Nomade, S., Leung, K.N., and Lou, T.P., 2005. Application of
732 deuterium-deuterium (D-D) fusion neutrons to $^{40}\text{Ar}/^{39}\text{Ar}$ geochronology. *Applied Radiation*
733 *and Isotopes* 62, 25-32.
- 734 Renne, P.R., Mundil, R., Balco, G., Min, K.W., and Ludwig, K.R., 2010. Joint determination
735 of ^{40}K decay constants and $^{40}\text{Ar}^*/^{40}\text{K}$ for the Fish Canyon sanidine standard, and
736 improved accuracy for $^{40}\text{Ar}/^{39}\text{Ar}$ geochronology. *Geochimica et Cosmochimica Acta* 74,
737 5349-5367.
- 738 Renne, P.R., Balco, G., Ludwig, K.R., Mundil, R., and Min, K., 2011. Response to the
739 comment by W.H. Schwarz et al. on " Joint determination of ^{40}K decay constants and ^{40}Ar
740 $^*/^{40}\text{K}$ for the Fish Canyon sanidine standard, and improved accuracy for $^{40}\text{Ar}/^{39}\text{Ar}$
741 geochronology " by PR Renne et al. (2010). *Geochimica et Cosmochimica Acta* 75, 5097-
742 5100.
- 743 Renne, P.R., and Norman, E.B., 2001. Determination of the half-life of ^{37}Ar by mass
744 spectrometry. *Physical Review C* 63.
- 745 Renne, P.R., Sharp, W.D., Deino, A.L., Orsi, G., and Civetta, L., 1997. $^{40}\text{Ar}/^{39}\text{Ar}$ dating into
746 the historical realm: Calibration against Pliny the Younger. *Science* 277, 1279-1280.
- 747 Renne, P.R., Swisher, C.C., Deino, A.L., Karner, D.B., Owens, T.L., and DePaolo, D.J., 1998.
748 Intercalibration of standards, absolute ages and uncertainties in $^{40}\text{Ar}/^{39}\text{Ar}$ dating. *Chemical*
749 *Geology* 145, 117-152.
- 750 Renne, P.R., WoldeGabriel, G., Hart, W.K., Heiken, G., and White, T.D., 1999.
751 Chronostratigraphy of the Miocene-Pliocene Sagantole Formation, Middle Awash Valley,
752 Afar rift, Ethiopia. *Geological Society of America Bulletin* 111, 869-885.
- 753 Shuster, D.L., Flowers, R.M., and Farley, K.A., 2006. The influence of natural radiation
754 damage on helium diffusion kinetics in apatite. *Earth and Planetary Science Letters* 249,
755 148-161.
- 756 Singer, B.S., Dungan, M.A., and Layne, G.D., 1995. Textures and Sr, Ba, Mg, Fe, K and Ti
757 compositional profiles in volcanic plagioclase - clues to the dynamics of calc-alkaline
758 magma chambers. *American Mineralogist* 80, 776-798.

- 759 Singer, B.S., Wijbrans, J.R., Nelson, S.T., Pringle, M.S., Feeley, T.C., and Dungan, M.A.,
760 1998. Inherited argon in a Pleistocene andesite lava: $^{40}\text{Ar}/^{39}\text{Ar}$ incremental-heating and
761 laser-fusion analyses of plagioclase. *Geology* 26, 427-430.
- 762 Solomatov, V.S., 1995. Batch crystallization under continuous cooling - analytical solution for
763 diffusion-limited crystal-growth. *Journal of Crystal Growth* 148, 421-431.
- 764 Stoenner, R.W., Schaeffer, O.A., and Katcoff, S., 1965. Half-lives of argon-37 argon-39 and
765 argon-42. *Science* 148, 1325-1328.
- 766 Wartho, J.A., Kelley, S.P., Brooker, R.A., Carroll, M.R., Villa, I.M., and Lee, M.R., 1999.
767 Direct measurement of Ar diffusion profiles in a gem-duality Madagascar K-feldspar
768 using the ultra-violet laser ablation microprobe (UVLAMP). *Earth and Planetary Science*
769 *Letters* 170, 141-153.
- 770 Zeitler, P.K., 1987. Argon diffusion in partially outgassed alkali feldspars - insights from
771 $^{40}\text{Ar}/^{39}\text{Ar}$ analysis. *Chemical Geology* 65, 167-181.
- 772 Zellmer, G.F., and Clavero, J.E., 2006. Using trace element correlation patterns to decipher a
773 sanidine crystal growth chronology: An example from Taapaca volcano, Central Andes.
774 *Journal of Volcanology and Geothermal Research* 156, 291-301.

775

776 **Figure Captions**

777

778 Figure 1. Continuous laser $^{40}\text{Ar}/^{39}\text{Ar}$ results. (A) Age spectra for individual sanidine
779 phenocrysts. (B) Age spectra for replicate aliquots of amphibole phenocrysts. (C) Age
780 probability plot for individual dense (Ba-rich) fragments of alkali feldspar overgrowths.

781

782 Figure 2. Laser ablation $^{40}\text{Ar}/^{39}\text{Ar}$ results for two traverses, one (filled symbols) along the
783 surface of a one grain and one (open symbols) across an interior surface of another grain
784 broken to reveal the core. Uncertainties in traverse distances are $\pm 50 \mu$.

785

786 Figure 3. Backscattered electron (BSE) images of alkali feldspar phenocrysts. Brightness
787 reflects elevated Ba concentrations. Note dark, partially resorbed cores (xenocrysts) in each
788 phenocryst and variably complex zoning in overgrowths.

789

790 Figure 4. Ba concentration (atoms per formula unit) in various profiles measured along linear
791 reconnaissance traverses in six different feldspar grains. Traverses are approximately normal to
792 the traces of compositional zone boundaries. All data were acquired with a 15 kV beam. Colors
793 distinguish traverses in a given grain, and different symbols distinguish different traverses.
794 Distance scales for each traverse begin and end at arbitrary positions, but each distance scale
795 increases from interior to exterior portions of the grains. Portions of profiles with <0.03 Ba
796 APFU are from cores (xenocrysts).

797

798 Figure 5. Ternary representation of feldspar compositions, combining anorthite (An) and
799 celsian (Cn) components, with symbols as indicated.

800

801 Figure 6. Core to rim electron microprobe traverse across grain G15 (see Figure 3) showing
802 variations in Ba, Sr, K, Na and Ca in units of cations per formula unit (8 oxygen atoms).

803

804 Figure 7. Effects of varying acceleration voltage on excitation volume in parallel traverses
805 across a contact between core and overgrowth in grain G13. Two traverses (A and B) were
806 made at 10 kV. The larger excitation volume at 15 and 20 kV produces gentler profiles across
807 the contact, spuriously implying more extensive diffusion. Differences in Ba concentration of
808 the overgrowth at ~ 2 -5 mm from the contact are due to lateral variations along the contact.
809 These data were not used for diffusion couple modeling. All data used for diffusion modeling
810 were acquired at 10 kV.

811

812 Figure 8. Effects of varying orientation of traverse relative to trace of interface between cores
813 and overgrowths, measured on grain G15. Relationships are shown schematically in the inset,
814 which shows three traverses in plan view of thin section across a vertical compositional
815 boundary. The highly oblique traverse provides highest spatial resolution. Distances are
816 subsequently projected to orthogonal coordinates. Data used for diffusion modeling were
817 acquired at 59° from normal.

818

819 Figure 9. Electron microprobe traverses (2σ data point errors) across selected boundaries in
820 the grains indicated, shown with least squares fitted diffusion profiles (red curves with

821 dashed error envelopes). Traverses identified with subscripted 0 (e.g., G15₀) are from the
822 contact between a xenocryst core and the innermost overgrowth zone. Values of Dt and
823 their uncertainties, computed from the regression and corrected for excitation volume
824 effects, are shown.

825

826 Figure 10. Permissible time-temperature square-pulse heating scenarios that predict the Ba
827 diffusion profiles (colored bands bounded by error limits) compared with time-temperature
828 square-pulse heating scenarios that predict 10–90% $^{40}\text{Ar}^*$ loss (green curves; calculated for
829 three different diffusion radii (r) as indicated). The vertical band centered at 879°C shows the
830 magma temperature and range inferred from two-feldspar thermometry. The intersection of the
831 vertical band (the inferred magma temperature) and the colored bands (the permissible time-
832 temperature histories constrained by the Ba diffusion profiles) defines the magma residence
833 time. The mutual intersection of the two aforementioned bands with a green curve defines the
834 predicted fractional loss of $^{40}\text{Ar}^*$ due to magma residence. Fractional $^{40}\text{Ar}^*$ loss curves are
835 calculated from diffusion data summarized by (Lovera et al., 1997), with mean values of
836 activation energy ($E_a = 46 \pm 6$ kcal/mol) and pre-exponential factor $\log(D_0/r_0^2) = 5 \pm 3$.
837 Fractional loss curves are shown for diffusion parameters one standard deviation higher and
838 lower than these mean values, representing lower and upper bounds (respectively) on argon
839 retentivity. The fractional loss curves in panels (a-c) correspond to $E_a = 40$ kcal/mol and
840 $\log(D_0/r^2) = 2$. Those in panels (d-f) correspond to $E_a = 52$ kcal/mol and $\log(D_0/r^2) = 8$.

ACCEPTED MANUSCRIPT

Table 1. XRF Data

Major and Minor Element Oxides (Wt.-%)	
SiO ₂	52.33
TiO ₂	0.72
Al ₂ O ₃	21.45
FeO*	3.47
MnO	0.18
MgO	0.47
CaO	3.18
Na ₂ O	7.62
K ₂ O	5.67
P ₂ O ₅	0.11
LOI	4.32
Sum	99.51

Trace Elements (ppm)

Ni	3
Cr	3
Sc	1
V	43
Ba	2401
Rb	140
Sr	1503
Zr	303
Y	25
Nb	149
Ga	20
Cu	3
Zn	94
Pb	20
La	117
Ce	195
Th	21
Nd	54
U	3

